# Multiscale Model for Temperature Distribution in Hydrating Concrete

## V. Šmilauer & T. Krejčí

*Faculty of Civil Engineering, Department of Mechanics, Czech Technical University in Prague, Thákurova 7, 166 29 Prague 6, Czech Republic*

## ABSTRACT

*Temperature rise in hydrating concrete presents a formidable problem that may lead to significant acceleration of hydration kinetics, early-age cracking, and decreased durability. Multiscale formulation is proposed, coupling a cement hydration model on the microscale with the finite element method (FEM) heat conduction problem on the macroscale. Although discrete hydration model predicts heat evolution controlled by macroscale temperature, the FEM satisfies heat balance equation during thermal conduction. Two- and three-dimensional validations show a reasonable temperature conformity with an access to the local quantities, such as a degree of hydration.*

*Address all correspondence to vit.smilauer@fsv.cvut.cz, Phone 420-224-354-369

# 1. INTRODUCTION

Concrete performance is affected by temperature history in many ways. With no regard to well-controlled laboratory conditions, the mixing, placing, and curing of concrete occur worldwide under various environmental conditions. The understanding of underlying phenomena during concrete maturing and performance follows different attitudes of material and civil engineers and, in fact, presents a multiscale and interdisciplinary approach.

From a material point of view, concrete is a living heterogeneous material whose microstructure formation is considerably affected by temperature. It was recognized that higher curing temperature speeds up the rate of reactions and promotes high early strength [1]. However, such microstructure is characteristic by inhomogeneous placing of hydrates, coarser porosity, and higher density of calcium silicate hydrates (C-S-H) [2], resulting in a decreased long-term strength and durability. The recent advancement in high-strength concrete, utilization of secondary cementitious materials (SCM), and the use of admixtures has made the issue of concrete material even more complex [3].

The prediction of thermal stresses based on temperature history is a well-established concept in the framework of structural mechanics. A low thermal conductivity of concrete, the exothermic hydration process, and surrounding temperature cause temperature gradients accompanied by strains, especially in massive concrete elements. During the concrete cooling, tensile stresses often appear due to minor restraints in the system, which may lead to a microcrack formation and decreased durability [4, 5].

Several researchers formulated predictive models for temperature evolution under adiabatic condition, in the form of exponential function [6] or hydration model [7]. Proper validation became a stepping stone for a multiscale approach, recognizing the heterogeneous temperature distribution on the macroscale. The phenomenological hydration model [8] or later the more sophisticated affinity hydration model [9] have been previously employed in the coupled micro/macrothermal analysis.

The formulation of fully coupled thermochemo-mechanical models was nevertheless proposed [10–13] and is remarkable for the amount of input parameters. Several of them have to be obtained experimentally, thus weakening the potential for a general-purpose tool.

Instead of direct modeling of the crack formation using highly sophisticated models, engineers often proposed guidelines to produce high-quality concrete satisfying elementary rules [1, 14]. Such an approach does not require detailed modeling and relies more on experience and expertise. For example, the temperature anywhere in the concrete element should not exceed 70°C during hardening to avoid possible risk of delayed ettringite formation accompanied by expansion [15]. The cooling rate should not exceed 3°C/h during the first 24 h and special caution is necessary in cold weather when concrete temperature falls bellow 4°C [14].

Proposed simulation methodology relies on a multiscale concept, introducing two separable scales, as follows:

1. **Cement paste level** found on the scale between 1 and 100 µm. Clinker minerals, gypsum, CH[1], CSH, other minor phases, and capillary porosity are present,

2. **Structural level** represents the span from centimeter up to several meters. Concrete found at this level is comprised mainly from cement paste, SCM as well as fine and coarse aggregates. The topology of concrete structure with assigned boundary conditions complements material information.

A thermochemical multiscale model is formulated to predict realistic temperature evolution and distribution in arbitrary concrete member under varying boundary conditions. The emphasis is given on the material scale, taking into account cement chemical and physical properties. A discrete CEMHYD3D hydration model based on cellular automata is used to simulate microstructure evolution of hydrating cement paste [16]. A conventional transient heat conduction problem is solved through the finite element method (FEM) at the macroscale level [17]. The formulation relies on intrinsic material data, such as reaction enthalpy, resulting in a versatile and extensible engineering tool.

---

[1] Using standard notation of cement chemistry.

## 2. CEMENT HYDRATION MODEL ON THE MICROSCALE

The microscale of cement paste is a stepping stone for multiscale analysis, relying on the assumption that aggregates do not contribute significantly to the cement hydration process. Therefore, the heat evolution of concrete may be linked directly to the cement paste level. Any hydration model designed for the prediction of heat release has to capture underlying chemical reactions as well as the topology of cement grains. The latter controls the initial surface area of cement grains with the consequences to hydration kinetics and later stages of hydration due to the deposition of hydrates typically around cement grains, preventing capillary water from further reaction. Hydration modeling is based on an open-source, discrete hydration model CEMHYD3D [16], allowing one to include directly the following:

- particle size distribution of cement

- chemical composition of cement ($C_3S$, $C_2S$, $C_3A$, $C_4AF$, gypsum)

- actual temperature and its history

- water regime (under saturated and sealed conditions)

- water-to-cement ratio ($w/c$) and the amount of cement in concrete

- supplementary cementitious materials (silica, slag, fly ash)

The microstructure of cement paste, referred to as a representative volume element (RVE) [18], is approximated in the CEMHYD3D model by voxels with the size of $1 \times 1 \times 1$ μm. Each of them represents one chemical phase, either in solid or dissolved state. Figure 1 shows an example of initial and well-hydrated RVE of $50 \times 50 \times 50$ μm. The initial periodic RVE is reconstructed by throwing digital spheres following cement particle size distribution (PSD). Assessment of real cement PSD is usually not available; hence, it becomes more convenient to express PSD curve by a single and accessible variable–Blaine fineness. Rosin-Rammler cumulative distribution $G(d)$ was fitted to a NIST reference database for Dyckerhoff cements, see [16], with the results

$$G(d) = 1 - e^{-bd^n}, \quad \lim_{d \to \infty} G(d) = 1 \qquad (1)$$

$$n = -8.333 \times 10^{-4} \text{ fineness} + 1.1175 \qquad (2)$$

$$b = 7.54 \times 10^{-4} \text{ fineness} - 0.143 \qquad (3)$$

where $d$ (in microns) is the particle diameter and Blaine fineness is expressed in meters squared per kilogram. Figure 2 displays cumulative distribution for coarse and fine cements with corresponding Blaine fineness of 250 and 500 m$^2$/kg, according to Eqs. (1)–(3). The amount of cement in the RVE is controlled by $w/c$ and gypsum content.
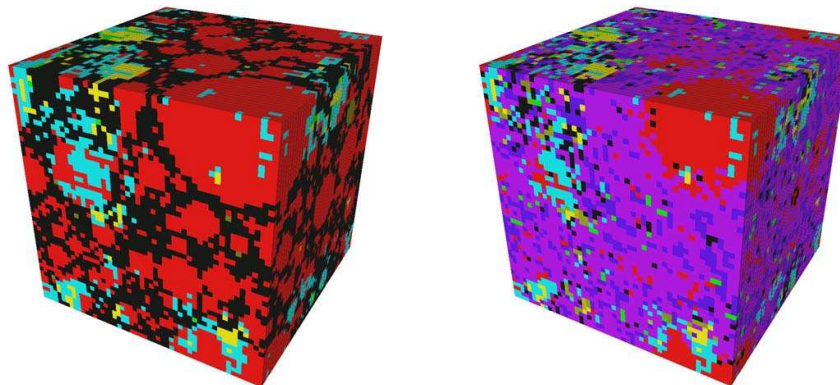


**FIGURE 1.** RVE $50 \times 50 \times 50$ μm, $w/c = 0.25$, initial **(left)** and at the degree of hydration of 0.63 **(right)**. Dominant phases include water-filled porosity (black), $C_3S$ (red), $C_2S$, $C_3A$, $C_4AF$, gypsum, CH (blue), and C-S-H (violet)
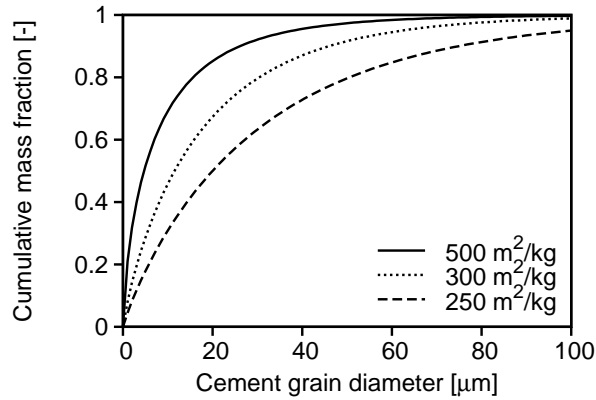
**FIGURE 2.** Assumed Rosin-Rammler cumulative distribution for cements with three Blaine finenesses according to Eqs. (1)–(3)

The chemical reactions are modeled on the basis of cellular automata rules, describing the process of dissolution, transport, nucleation, and reaction. Liberated heat is calculated directly from evolving microstructure assigning enthalpy to each chemical reaction [7]. For example, the hydration of the most common mineral $C_3S$ of Portland cement yields 517 J/g of dissolved $C_3S$

$$C_3S(1) + 5.3H(1.34) \rightarrow C_{1.7}SH_4(1.52)$$
$$+ 1.3CH(0.61) \tag{4}$$
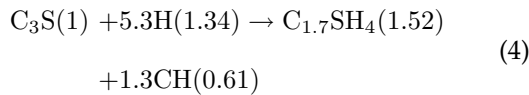
where the numbers in parenthesis correspond to reaction volumes at 20°C. In the model, saturated or sealed curing conditions are considered with no further moisture effect on hydration. Such simplification is supported by the fact that relative humidity (RH) seldom drops below 90% even in exterior parts within a few days when exposed to ambient 60% RH [1]. Therefore, a sealed curing boundary condition is a realistic assumption when no considerable water evaporation takes place. If the RH drops below approximately 80% RH, them the hydration ceases.

The temperature effect on hydration kinetics is determined from Arrhenius equations simultaneously for all implemented reactions. The characteristic time $\tau$ is modified according to the maturity principle [19]

$$\tau(T) = \tau(T_0) \exp\left[\frac{E_a}{R}\left(\frac{1}{T_0} - \frac{1}{T}\right)\right] \tag{5}$$

where $T_0 = 298.15$ K is a reference temperature, $T$ corresponds to arbitrary homogeneous temperature, $R = 8.314$ $\text{Jmol}^{-1}\text{K}^{-1}$ represents the universal gas constant and $E_a$ stands for an apparent activation energy, for ordinary Portland cement typically around 40 $\text{kJmol}^{-1}$ [20]. Equation (5) proves a strong temperature effect on heat release rate (e.g., going from 25 to 50°C is a speedup factor of 3.5 for hydration progress and heat release rate).

The cycles in cellular automata represent no meaningful scale of time. Original linear mapping of cycles showed considerable disagreement with experiments [21]. Parabolic mapping, based on the Knudsen's parabolic dispersion model, was found appropriate under different curing conditions and cement types [22]. Knudsen's model assumes that the diffusion of ions takes the control over the hydration rate

$$\tau = t_0 + \beta \, \text{cycle}^2 \tag{6}$$

The parameter $\beta$ is usually found in the interval $1 \times 10^{-4} \leq \beta \leq 1.1 \times 10^{-3}$ $\text{h/cycle}^2$ [22, 23], while $t_0$ represents extra dormant time. Both parameters contain the influence of admixtures, alkalis, cement impurities, etc. A standard induction period of Portland cement is included directly in the hydration modeling and sets $t_0 = 0$ h.

The size of RVE plays a fundamental role in the calculations [24]. For the cement hydration, one has to consider at least the effect of truncated PSD, cement fineness, and $w/c$. The maximum accommodated particle diameter must be truncated to approximately half of RVE edge to allow finer grain placement (i.e., to maximum diameter 5 μm at $10 \times 10 \times 10$, 25 μm at $50 \times 50 \times 50$ μm, and 50 μm at $100 \times 100 \times 100$ μm). Coarse cement with high $w/c$ is the most susceptible combination, where truncation and PSD renormalization creates in fact a fine cement (Fig. 2).

To shed a light on the effect of RVE size, five random realizations were generated for ordinary coarse Portland cement with Blaine fineness 250 $\text{m}^2/\text{kg}$ and $w/c = 0.5$. Figure 3 displays the evolution of degree of hydration, tightly related to released heat. Hydration at 20°C shows that $10 \times 10 \times 10$ μm proceeds faster due to truncated large particles than reference at $100 \times 100 \times 100$ μm. The reasonable selection is $50 \times 50 \times 50$ μm for the scatter and computational speed.
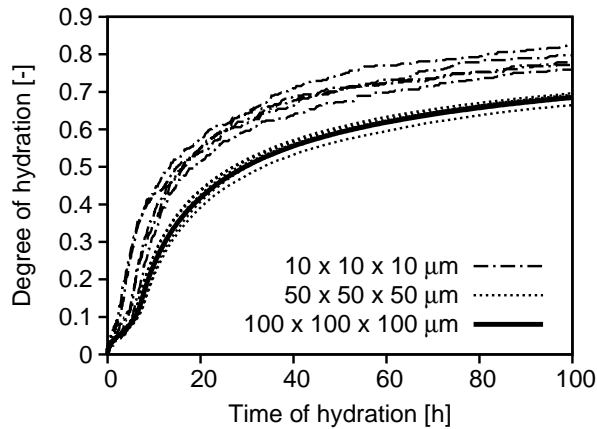
**FIGURE 3.** Effect of RVE sizes on degree of hydration, each with five random realizations

Nowadays, SCM such as slag or fly ash are blended with Portland cement due to economical, ecological, and durability reasons. The common level of substitution reaches up to 35% by mass, although much higher replacements may exist [1]. The consequence is decreased potential heat of blended cement with slow transformation of secondary binders to hydration products. Because of very low heat contribution, if any, from the reaction of SCM generally occurs during the first hydration days [25–28], the SCM are considered as an inert filler in the simulations.

## 3. HEAT TRANSPORT ON THE STRUCTURAL SCALE

Transient three-dimensional (3D) heat conduction is solved on the structural scale. Energy balance on a differential element yields [17, 29]

$$-\nabla^T \mathbf{q}(\mathbf{x}) + \overline{Q}(\mathbf{x}, t) = \rho(\mathbf{x}) c_p(\mathbf{x}) \frac{\partial T(\mathbf{x}, t)}{\partial t} \quad (7)$$

where $\mathbf{q}(\mathbf{x})$ (in Watts per meters squared) is a heat flux originating in conduction, convection, or radiation, $\overline{Q}(\mathbf{x}, t)$ [W/m$^3$] represents given heat source from the CEMHYD3D model, $\rho(\mathbf{x})$ (in kilograms per cubic meter) stands for a concrete density, $c_p(\mathbf{x})$ [Jkg$^{-1}$K$^{-1}$] is a specific heat capacity and $T(\mathbf{x}, t)$ (in degrees Kelvin) represents unknown temperature field.

The introduction of Fourier's law into Eq. (7) leads to the formulation of 3D heat conduction equation in terms of temperature field

$$\lambda(\mathbf{x}) \Delta T(\mathbf{x}) + \overline{Q}(\mathbf{x}, t) = \rho(\mathbf{x}) c_p(\mathbf{x}) \frac{\partial T(\mathbf{x}, t)}{\partial t} \quad (8)$$

where $\lambda(\mathbf{x})$ (in Watts per meter per degree Kelvin) is a thermal conductivity of isotropic material.

Dirichlet's, Neumann's, or Cauchy's boundary conditions can be associated with Eqs. (7) and (8). Treatment of heat convection on a concrete surface is conveniently described by Newton's law

$$\mathbf{n}(\mathbf{x})^T \mathbf{q}(\mathbf{x}) = h(\mathbf{x}) \left( T(\mathbf{x}) - T_\infty \right), \quad \mathbf{x} \in \Gamma_c \quad (9)$$

where $\mathbf{n}(\mathbf{x})$ is a unit normal vector pointing outwards from the surface, $h(\mathbf{x})$ is a heat transfer coefficient and $T_\infty$ is the ambient temperature far enough from the boundary layer. The solution of Eq. (8) requires prescribed initial temperature $\overline{T}(\mathbf{x}, 0)$ over the body

$$T(\mathbf{x}, 0) = \overline{T}(\mathbf{x}, 0), \quad \mathbf{x} \in \Omega \quad (10)$$

The analytical solution of Eq. (8) is not amenable for more complicated cases. Instead, FEM is employed, starting with the formulation of a weak problem [17]. A linear set of algebraic equations will be obtained in the form

$$C\dot{\mathbf{r}} + K\mathbf{r} = \mathbf{p} \quad (11)$$

where $\dot{\mathbf{r}}$ represents temperature nodal derivatives with respect to time, $C$ is a capacity matrix, and $K$ is a conductivity matrix [17]. The heat load vector $\mathbf{p}$ comprises heat flow on the boundary and heat source in the domain. The solution of the first-order transient problem of Eq. (11) can be accomplished by many techniques (e.g., finite differences or mode superposition). Here, the time domain is discretized by a time step

$$\Delta t_n = t_{n+1} - t_n, \quad n = 1, 2 \ldots (\text{time steps} - 1) \quad (12)$$

and the solution proceeds by the v-form of trapezoidal scheme [30]. Crank-Nicolson integration scheme is used further. It should be noted that heat source $\overline{Q}(\mathbf{x}, t_{n+1})$ is determined from average temperature at the previous time step $t_n$ thus bringing small inaccuracy which remains unbalanced in the calculation.

Figure 4 displays adopted coupling between two scales. The heat source $\overline{Q}(\mathbf{x}, t)$ represents the hydration heat of cement paste determined from the CEMHYD3D model. Because the temperature has a strong effect on released heat, it becomes necessary to couple hydration model on the microscale with the structural model on the macroscale in terms of temperature and liberated hydration heat.

Instead of having separate microstructures in each Gauss point, they can be assigned directly to finite element(s) or a broader selection. The temperature for CEMHYD3D is taken as an average from corresponding Gauss points. Such simplification is advantageous in reduced computational time when finite elements are expected to exhibit similar temperature field. However, the same heat power $\overline{Q}(\mathbf{x}, t)$ passed to associated macroscopic domain generally leads to underprediction of maximum temperature and overprediction of minimum temperature. Proper identification of elements with expected similar field is an important point when reduction in computational time is required.

The multiscale model is implemented in a general FEM open-source package TRFEL,[2] suited for transport problems.

## 4. THERMAL PROPERTIES OF CONCRETE

The simulation of heat conduction problems requires concrete heat conductivity, capacity and heat transfer coefficient. The hydration process changes the volume fraction of evaporable water, unhydrated cement, and hydrates. Therefore, thermal properties vary with concrete composition and degree of hydration. Figure 5 displays concrete conductivity for mature ordinary concrete depending on its unit mass and saturation conditions according to [1] and former Czech standard ČSN 731208. The latter considers 1.5 for dry and 1.7 $\mathrm{Wm^{-1}K^{-1}}$ for saturated concrete.

Concrete can be considered at the first approximation as a two-phase medium comprising cement paste and aggregates. Heat capacity of cement paste is significantly affected by the amount of water with heat capacity 4.18 $\mathrm{Jg^{-1}K^{-1}}$. The cement powder has typically 0.75 $\mathrm{Jg^{-1}K^{-1}}$ [31]. Detailed study discovered that fresh cement paste corresponds
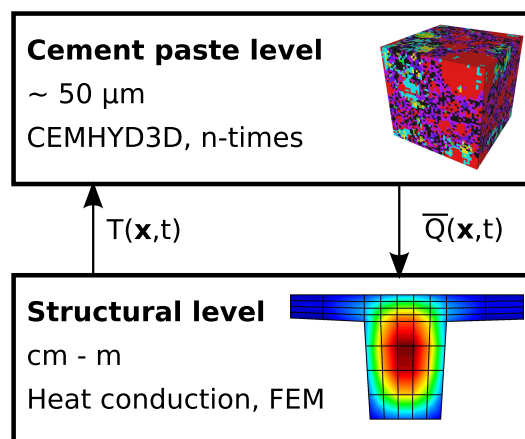


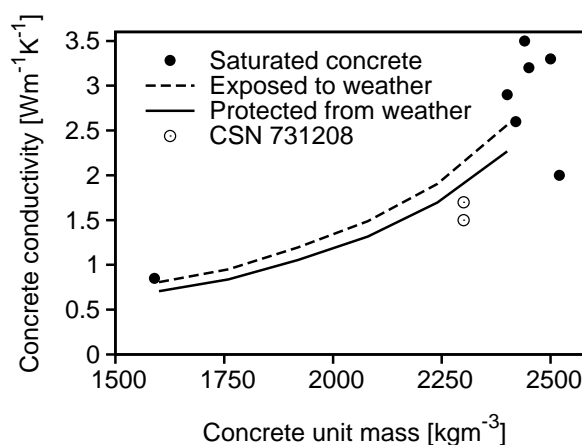**FIGURE 4.** Coupling between the level of cement paste and structure



**FIGURE 5.** Thermal conductivity of mature concrete according to a Czech standard and [1]

to heat capacities 1.55, 1.73, and 1.89 $\mathrm{Jg^{-1}K^{-1}}$ for $w/c = 0.3,\ 0.4$, and 0.5, respectively [31]. The law of mixture can be used for the estimation of heat capacity for concrete. Figure 6 shows heat capacity for cement paste according to [31] and for concrete containing 85% of granite aggregate by mass. Former Czech standard ČSN 731208 declares 0.84 and 0.87 $\mathrm{Jg^{-1}K^{-1}}$ for dry and saturated mature concrete, respectively.

Different heat transfer coefficients were reported in the literature, e.g., [9] considered $h = 11.63\ \mathrm{Wm^{-2}K^{-1}}$ for concrete exposed to air while
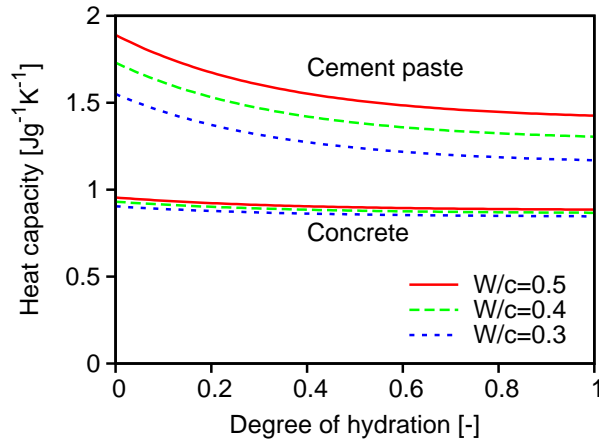
**FIGURE 6.** Heat capacity for cement paste and concrete predicted by the law of mixture

$h = 9.3 \ \mathrm{Wm^{-2}K^{-1}}$ for the surface surrounded by a plywood formwork. [8] used $h = 9.7 \ \mathrm{Wm^{-2}K^{-1}}$ for the heat transfer between formwork and ambient air. Table 1 summarizes heat transfer coefficient for concrete according to former Czech standard ČSN 731208. When concrete surface is covered with a thin layer of other material, such as a formwork, heat transfer coefficients add inversely. The overall heat transfer coefficient is approximated by a harmonic mean

$$h_i = \frac{\lambda_i}{t_i} \qquad (13)$$

$$\frac{1}{h} = \sum_{i=1}^{n} \frac{1}{h_i} = \frac{1}{h_1} + \frac{t_2}{\lambda_2} + \dots \qquad (14)$$

where $t_i$ represents the thickness of a layer.

## 5. VALIDATION

### 5.1 Isothermal Calorimetry of Cement Paste

Validation of hydration model starts on a paste prepared from ordinary Portland cement CEM I 42.5 R, produced at location Mokrá, Czech Republic. Cement was mixed with water at $w/c = 0.5$ and inserted in an isothermal calorimeter at 25°C. The CEMHYD3D model was calibrated for parameters $\beta$ and $t_0$ according to Eq. (6). Initial RVE $50 \times 50 \times 50$ μm was reconstructed and hydrated with input parameters summarized in Table 2.

**TABLE 1.** Heat transfer coefficient for concrete exposed to air or water according to the standard ČSN 731208

| Concrete in contact with | $h$ (Wm$^{-2}$K$^{-1}$) |
| --- | --- |
| air in enclosed environment | 8 |
| air during summer | 15 |
| air during winter | 23 |
| water | 31 |

The calibration provided $\beta = 7.8 \times 10^{-4}$ h/cycle$^2$ and $t_0 = 1.2$ h. Both the reference model and experimental temperatures are identical; hence, the activation energy is irrelevant. Results in Fig. 7 exhibit a good overall match. However, the discrepancy up to 10 hours is a consequence of simplified assumption in which the dissolution of clinker minerals is controlled by a power function of C-S-H [23]. An effect of electric double-layer, ion concentration, and autocatalytic nucleation of C-S-H is not incorporated directly and surely presents one of the most challenging tasks in the hydration modeling. An observed difference is acceptable for multiscale simulation because the majority of heat is released after initial period. Second discrepancy at later hydration stage is attributed to the sensitivity and stability of the calorimeter unit. Potential hydration heat $Q_{\mathrm{pot}}$, determined from $t = 130$ h, corresponds to realistic 520.5 J/g of cement.
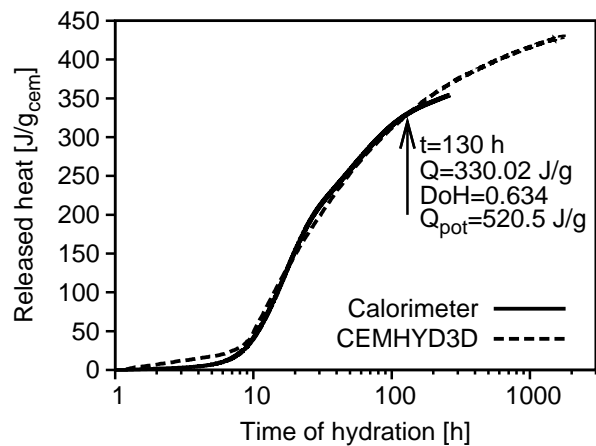


**FIGURE 7.** Isothermal calorimetry and CEMHYD3D simulation at 25°C, $w/c = 0.5$

**TABLE 2.** Cement properties and simulation parameters

| Component | $C_3S$ | $C_2S$ | $C_3A$ | $C_4AF$ | Gypsum |
|---|---|---|---|---|---|
| Mass content without gypsum | 0.612 | 0.126 | 0.070 | 0.10 | - |
| Normalized mass content without gypsum | 0.683 | 0.138 | 0.083 | 0.096 | - |
| Volume content with gypsum | 0.649 | 0.131 | 0.078 | 0.092 | 0.05 |
| Blaine fineness | 306 $m^2$/kg |
| Autocorrelation NIST files | cm115x2f |

## 5.2 Cube of Self-Compacting Concrete

The temperature evolution of self-compacting concrete was measured at Czech Technical University in Prague. A cube of $1 \times 1 \times 1$ m was casted at one step in the shelter, protecting the specimen from sun radiation and rain. Nine equally spaced temperature gauges were embedded in the horizontal direction across the cube thickness, the outer sensor was placed 30 mm from the surface (Fig. 8). Two temperature gauges measured ambient air temperature and all data were automatically gathered for the duration of at least six days.

The model description is given by Fig. 8. The top surface was in direct contact with atmosphere, therefore the heat transfer coefficient was chosen $h = 19$ Wm$^{-2}$K$^{-1}$ as the average between winter and summer season, Table 1. The thickness of formwork plywood in the vertical direction was 15 mm, therefore,

$$h = \left(\frac{1}{19} + \frac{0.015}{0.13}\right)^{-1} = 5.95 \text{ Wm}^{-2}\text{K}^{-1} \qquad (15)$$

During pilot simulation, the difference between the center and surface temperatures revealed the need to lower the heat transfer coefficient to the value of 2.0 Wm$^{-2}$K$^{-1}$. One of the reasons could be the disturbance of air boundary layer by the formwork steel ribs.

The cube was placed on an old massive concrete separated by 2 mm thick impregnated paper, therefore

$$h = \frac{\lambda}{t} = \frac{0.1}{0.002} = 50.0 \quad \text{Wm}^{-2}\text{K}^{-1} \qquad (16)$$

and the old concrete was considered to have the temperature of ambient air.

Symmetrical configuration allowed the simulation of a cube quarter only. The prism was meshed for $2 \times 2 \times 4 = 16$ quadratic brick elements, the mesh had 141 DoF. One CEMHYD3D model was assigned to each finite element. The time integration step was fixed as 10 min.
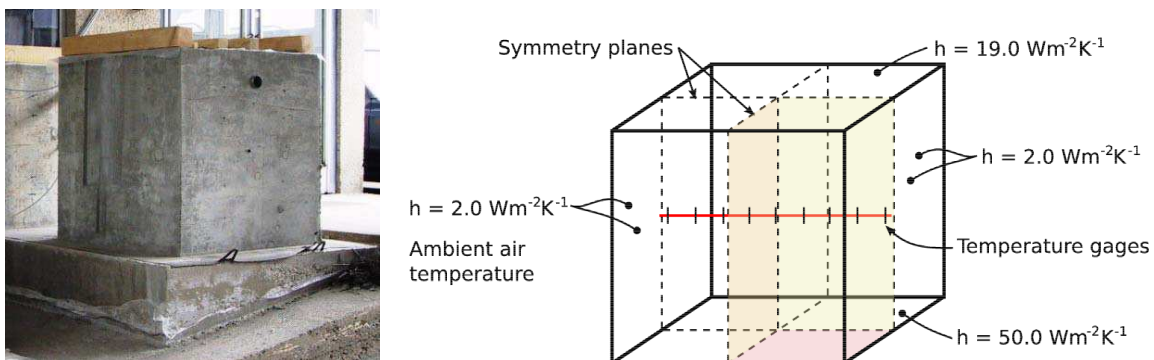


**FIGURE 8.** Experimental setup of a temperature measurement and corresponding quarter model (photo J. Litoš)

The concrete was composed from CEM I 42.5 R by the amount of $310 \, \text{kg/m}^3$ with $w/c = 0.4$. Fly ash as a filler was added further to the mixture but was disregarded for the heat contribution. Because cement mineralogical properties were unknown, data for initial microstructure were taken from Table 2 from an ordinary Portland cement of the same grade with the activation energy $E_a = 38.3 \, \text{kJ/mol}$. Thermal conductivity of concrete was assumed constant $1.7 \, \text{Wm}^{-1}\text{K}^{-1}$, its capacity constant $0.84 \, \text{Jg}^{-1}\text{K}^{-1}$, and density $2.5 \, \text{t/m}^3$.

Figure 9 shows the temperature evolution in the middle of the cubic specimen and ambient air temperature. Following parameters were calibrated to match experimental data; $t_0 = 0$ h and $\beta = 6.3 \times 10^{-4}$ h/cycle$^2$. The maximum temperature in the center reached $50.17°\text{C}$ at 25.6 h and the simulation predicted $50.3°\text{C}$. Maximum temperature achieved 30 mm from the surface was $45.23°\text{C}$, and the simulation predicted $44.3°\text{C}$. The cooling stage after approximately two days shows overprediction by the simulation and emphasizes the role of heat transfer coefficients. Some heat could have dissipated from water evaporation, which was not taken into account.

Figure 10 shows the contour fill of the prism viewed from the central direction during the maximum center temperature at 25.6 h. Total computational time took 70 min on 3.2 GHz PC with optimized g++ compilation. Profiling showed that 98.5% of the whole computational time is taken by the CEMHYD3D routine. In such a case, the refinement of an integration time step does not create any time savings.
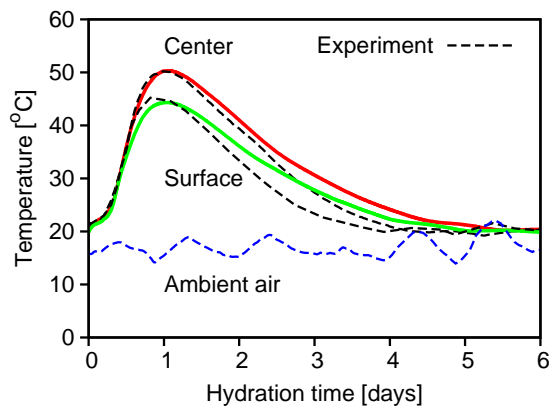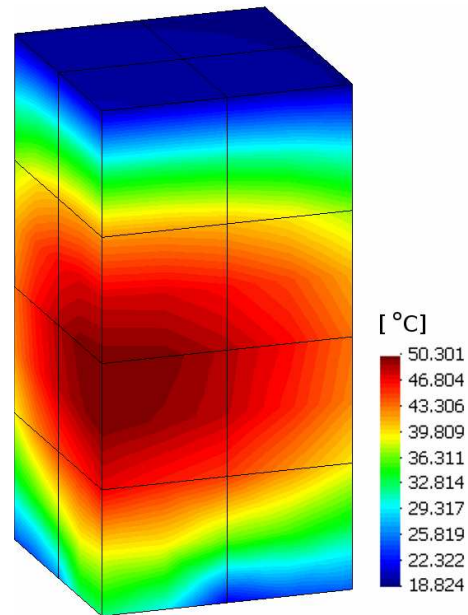


**FIGURE 10.** Contour fill of temperature field at 25.6 h when maximum temperature was achieved. A view from the central part of the quarter model

## 5.3 Prestressed Bridge

A new scaffold bridge was built during 2006–2007 in Prague. The bridge is a continuous beam of 12 spans made from prestressed concrete with the total length of 443 m.

The first simulation deals with the casting of bottom slab of the thickness of 0.697 m with a precast shoulder. The mesh was generated by T3D[3] software with resulting 215 nodes, 4 triangular, and 179 quadrilateral elements, together with 215 DoF (Fig. 11). The horizontal layered mesh structure was preferred due to CEMHYD3D assignment. Each layer of 20 elements has a similar temperature field; therefore, these elements are grouped to eight independent CEMHYD3D models according to Fig. 11.

The casting began at 10:00 on June 6, 2006. Initial temperature of casted concrete was measured in the interval 14.1–15.7°C and therefore was set to an initial 15°C together with the precast shoulder. Both the casted concrete and the precast shoulder



**FIGURE 9.** Validated heat evolution in the $1 \times 1 \times 1$ m specimen

---

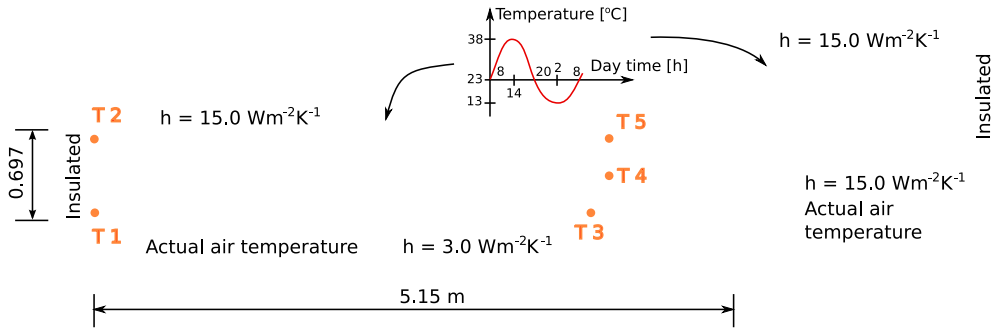[3] http://mech.fsv.cvut.cz/~dr/t3d.html

**FIGURE 11.** Mesh and boundary conditions of bottom slab. Different colors represent eight CEMHYD3D material models, the right shoulder is of mature precast concrete

were given the constant material parameters, thermal conductivity $1.7~\mathrm{Wm^{-1}K^{-1}}$ and heat capacity $0.84~\mathrm{Jg^{-1}K^{-1}}$. Used concrete composition with $w/b = 0.425$ is summarized in Table 3.

Pilot simulation revealed that the amount of Portland cement is excessive and has to be reduced to the minimum value according to EN 197-1 (i.e., 280 kg of pure Portland cement and 20 kg of inert SCM admixtures, yielding $w/c = 170/380 = 0.4473$). Input parameters were assumed according to Table 4. Mapping of hydration cycles to real time was calibrated to the temperature evolution of central T4 yielding $t_0 = 0$ h and $\beta = 5.6 \cdot 10^{-4}$ h/cycle$^2$.

Boundary conditions were set according to Fig. 11. While the bottom part was set to measured air ambient temperature, the temperature of the top surface, exposed to sun radiation, was approximated by

$$T(t) = 23 + \left[ 10 + 5H \left( \sin \left\{ 2\pi t + \frac{4\pi}{24} \right\} \right) \right]$$
$$\times \sin \left\{ 2\pi t + \frac{4\pi}{24} \right\} \tag{17}$$

where $H$ is a Heaviside step function and time $t$ is in days relatively to the beginning of casting. The maximum air temperature was considered at 14.00 h according to the measured data.

Similar location of gauges T1–T3 and T2–T5 gives very similar evolution of temperatures. Results for inner gauge T4 and ambient air temperature are plotted in Fig. 12; Fig. 13 shows gauges T3, T5. The inner part of casted massive concrete is close to adiabatic condition and influenced to a minor extent

**TABLE 3.** Concrete composition used in the simulation of the bridge, $w/b= 0.425$

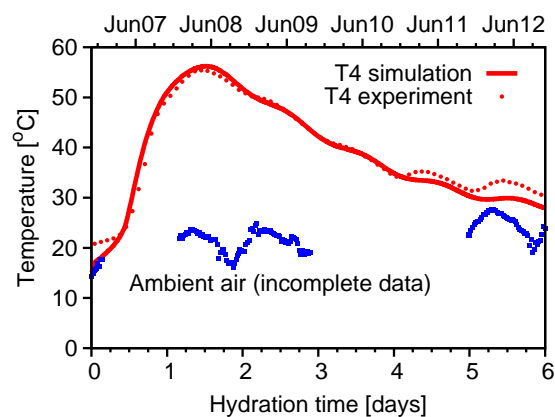| Concrete parameter | Value |
|---|---|
| Type | C35/45-XF2 |
| Cement (CEM I 42.5 R + SCM) | 380+20 kg/m$^3$ |
| Water | 170 kg/m$^3$ |
| Fine aggregates | 1100 kg/m$^3$ |
| Coarse aggregates | 450 kg/m$^3$ |
| Fly ash | 200 kg/m$^3$ |
| Superplasticizer | 3.6 kg |
| Bulk density | 2.32 kg/m$^3$ |



**FIGURE 12.** Temperature of central gauge T4 and ambient air temperature

by boundary conditions. Therefore, the correspondence between simulation and experiment reveals appropriate selection of material parameters. The data from ambient air temperature are incomplete,

TABLE 4. Cement properties and material simulation parameters

| Component | $C_3S$ | $C_2S$ | $C_3A$ | $C_4AF$ | Gypsum |
|---|---|---|---|---|---|
| Mass content without gypsum | 0.65 | 0.15 | 0.10 | 0.10 | - |
| Volume content with gypsum | 0.6175 | 0.1425 | 0.095 | 0.095 | 0.05 |
| Blaine fineness | 300 m$^2$/kg | | | | |
| Autocorrelation NIST files | 16130s1 | | | | |
| Activation energy $E_a$ | 38.3 kJ/mol | | | | |
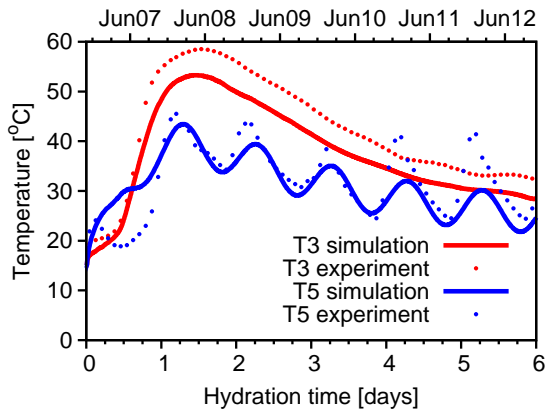


FIGURE 13. Temperature evolution in gauges T3 and T5

and the results between two points are interpolated in the simulation.

The maximum temperature 56.2°C was reached in gauge T4 at 1.53 day, and the temperature field is plotted in Fig. 14. Whole simulation took 57 min on 3.2 GHz PC and occupied 29 MB of RAM. Total simulation covered six days of hydration period with the constant time integration step 10 min.

Generally speaking, the difficulties of experimental data acquisition on rush construction site or several missing parameters tacitly or explicitly postu-

lated in the simulation lead logically to a scatter of the results. The disagreement in Figs. 12 and 13 up to 0.5 days rises speculations about gauge surrounding environment, gauge calibration, true initial mix temperature casted from several batches, etc. None of them can be proved, and the results are left as they were gathered. Another striking fact is a higher maximum measured temperature at the gauge T3 compared to the central gauge T4. Although such ambiguities might seem to falsify the simulation, results from a well-controlled small-scale experiments from Figs. 7 and 9 are convincing.

The new bridge beams had been casted on the bottom slab since July 12, 2006, 6:39 a.m. (i.e., after 35 days of bottom slab casting). The maximum beam width was 1.65 m and the maximum height reached 2.15 m. The generated mesh had 239 nodes, 39 triangular, and 177 quadrilateral elements with total 239 DoF. A simulated, typical cross section is depicted in Fig. 15 and allows another consideration of bridge symmetry vertical axis. Although the data from gauges T1–T5 were gathered from the bottom slab, only gauge T5 was considered important from maturing concrete slab. The mesh was adjusted in such a way that gauges T5–T10 were forced to be at a nodal position. The assignment of five hydration models with expected similar temperature field is displayed in Fig. 15.
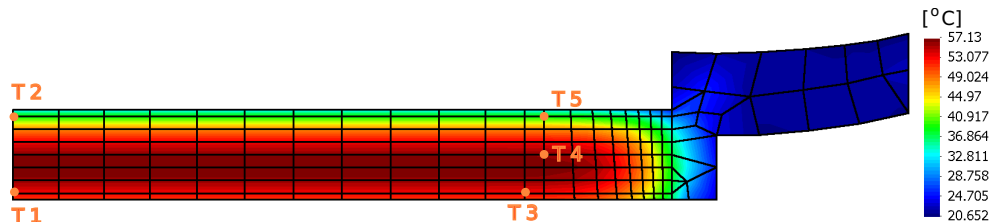


FIGURE 14. Contour fill at maximum temperature 56.2°C in gauge T4 after 1.53 day
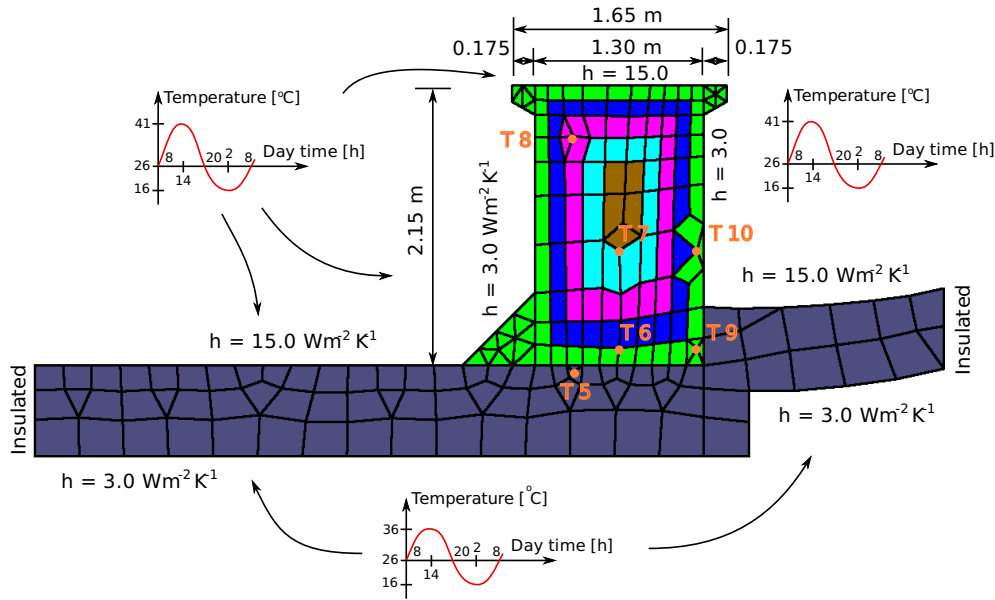
**FIGURE 15.** Topology and boundary conditions of the beam. Different colors represent different CEMHYD3D material models, the right shoulder and bottom slab are considered nonhydrating

The initial ambient air temperature was 26°C, while mature and fresh casted concrete reached 25°C. The bottom ambient air temperature was approximated by the function

$$T(t) = 26 + 10 \sin\left\{2\pi t - \frac{2.7\pi}{24}\right\} \qquad (18)$$

and the upper and vertical surfaces

$$T(t) = 26 + \left[10 + 5H\left(\sin\left\{2\pi t - \frac{2.7\pi}{24}\right\}\right)\right]$$
$$\times \sin\left\{2\pi t - \frac{2.7\pi}{24}\right\} \qquad (19)$$

Concrete and simulation parameters were set according to Tables 3 and 4. Further calibration modified $t_0 = 3$ h and $\beta = 4.0 \times 10^{-4}$ h/cycle$^2$ to match better results from central gauge T7. The pair gauges T6–T7, T9–T10 gave very similar experimental results; therefore, only gauges T5, T7, T10 were validated.

Results for the central gauge T7 are shown in Fig. 16. Maximum temperature was not measured directly due to power disconnection; how-
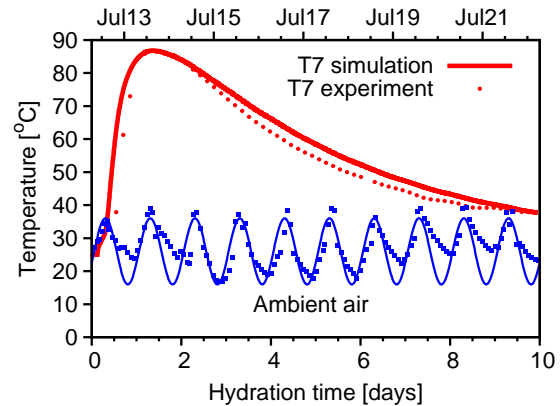


**FIGURE 16.** Temperature of central gauge T7 and approximated ambient air

ever, the simulated temperature reached a maximum of 86.8°C at 1.367 days (Figs. 16 and 18). Good accordance is achieved in T5 and T10 as well (Fig. 17). Both figures show a temperature underestimation probably due to lower heat transfer coefficients on the surfaces. Whole beam simulation took 68 min on 3.2 GHz PC and occupied 19 MB of RAM.
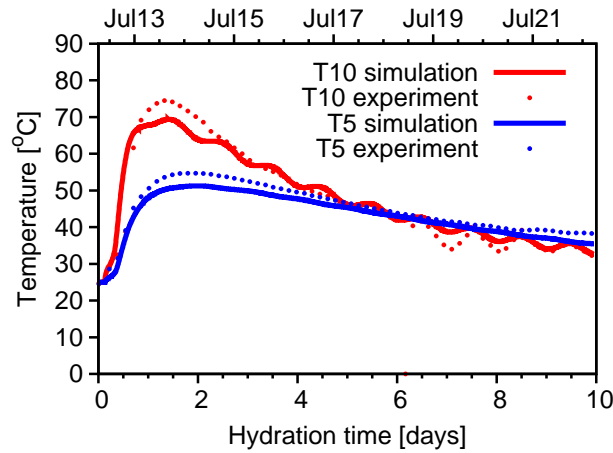
**FIGURE 17.** Temperature evolution in gauges T5 and T10
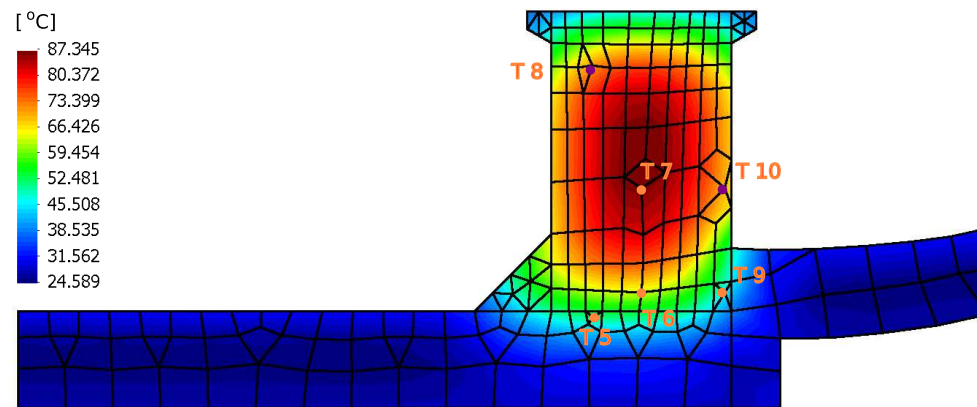


**FIGURE 18.** Temperature field at 1.367 days when the maximum in T7 is achieved

Calculations covered 10 days of the hydration period with a constant time integration step of 10 min using the Crank-Nicolson scheme.

The multiscale formulation allows accessing local quantities. The evolution of hydration degrees is depicted in Fig. 19 and demonstrates the effect of temperature history. The ultimate hydration degree approaches 0.8 due to low cement fineness, hence, the inability to hydrate large cement grains completely. Young's modulus can be predicted on the scale of cement paste and concrete. Here, the adopted analytical homogenization methodology is similar to [32], relying on intrinsic elastic properties of clinker minerals, hydration products and aggregates. In addition, homogenization includes the effect of interfacial transition zone, two types of C-S-H [33] and entrained air. Typical values complementing known concrete composition in Table 3 were used and the results are plotted in Fig. 20.

## 5.4 Role of Input Parameters at the Structural Level

The effect of individual input parameters on the resulting temperature field is explored in a closer detail. For this purpose, half of the bridge cross section in Fig. 21 was taken, capturing different thermal evolution in a massive beam and a slender
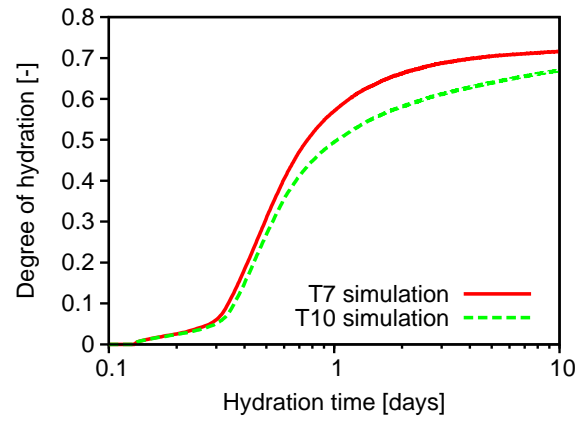
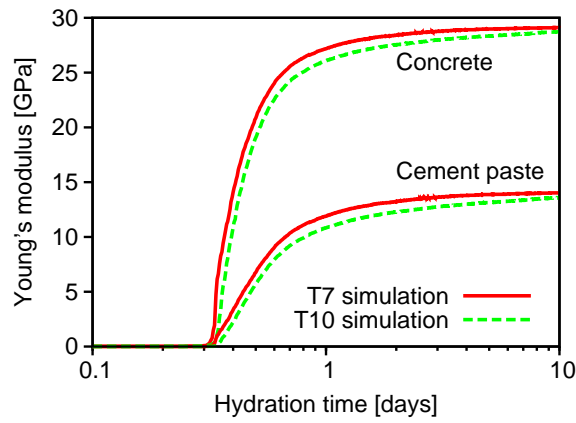**FIGURE 19.** Evolution of hydration degree in gauges T7 and T10



**FIGURE 20.** Predicted evolution of Young's modulus in gauges T7 and T10 on the scale of cement paste and concrete, no experimental data
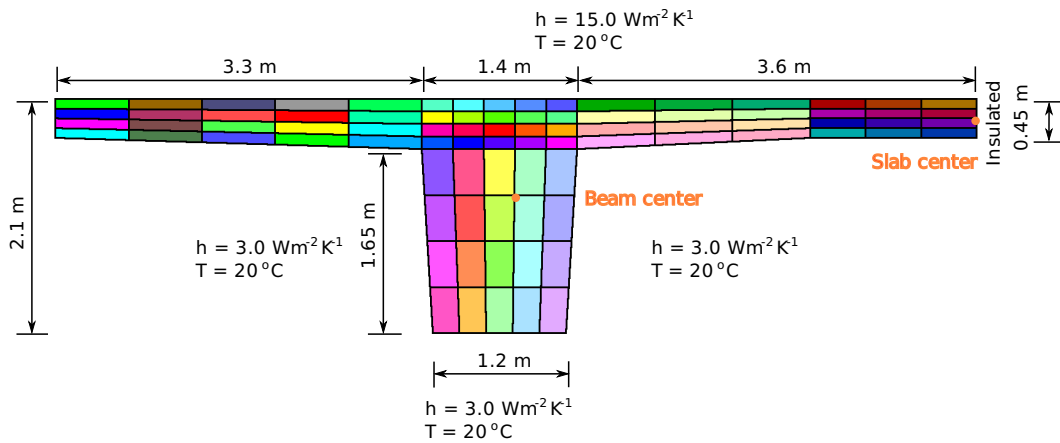


**FIGURE 21.** Topology of bridge cross section with the mesh, boundary conditions, and important node positions

slab. Each of 84 quadrilateral finite elements with linear interpolation corresponds to 84 independent CEMHYD3D material models. Because no great accuracy is expected, only $25 \times 25 \times 25$ μm microstructures were used. The macroscopic model has 109 DoF.

The starting "normal" concrete composition is made from 300 kg of CEM I 42.5 R according to Table 2 with assigned activation energy $E_a = 38.3$ kJ/mol and $w/c = 0.5$. Besides, the variation of other parameters covered as follows:

- 400 and 200 kg of cement CEM I 42.5 R

- increased Blaine fineness from 306 to 500 $m^2$/kg

- $C_3S$ increased from original 68.30% $C_3S$ to 73% by mass without gypsum, preserving the ratio of other clinker minerals and maintaining 5% of gypsum addition by volume

- $w/c$ decreased from 0.5 to 0.3

- initial mix temperature in the range from 0 to 30°C surrounded by 20°C ambient air temperature

Figure 22 indicates maximum temperatures in the beam and slab with corresponding elapsed time when $\beta = 7.8 \times 10^{-4}$ h/cycle$^2$ and $t_0 = 0.0$ h. As expected, massive beam with the dimensions $1.2 \times 2.1$ m is close to adiabatic curing conditions while the slab is progressively cooled down by ambient air. Cement in the amount of 200 kg/m$^3$ may represent not only pure Portland cement but a hydrating part of blended cements. Hydration at $w/c = 0.3$ is slowed down in later stages due to water demand, thus resulting in decreased reaction kinetics. A low initial mix temperature is very beneficial in preventing excessive overheating and, in fact, represents a common method found in various guidelines. A similar effect is expected from the surrounding ambient air temperature which would reflect casting in different seasons.

The maximum temperature in the beam is achieved between 40 and 100 h of hydration and demonstrates high influence of mix and curing conditions. Temperature in the slab 0.45 m thick is reached sooner for a given setup, approximately in the halftime of the beam (i.e., in the interval 20 and 47 h). It should be noted that the cycle-time mapping parameter $\beta$ could be lower, which would cause time shortening of maximum temperature.

The computation of one case took 46 min on 3.2 GHz PC and occupied 43 MB of RAM, including all code, data, and shared libraries. The simulation covered the period up to five days using a 10 min constant integration step.

## 6. CONCLUSION

A general multiscale heat conduction model for cement-based materials was developed and validated on small-size experiments, large bridge slab,
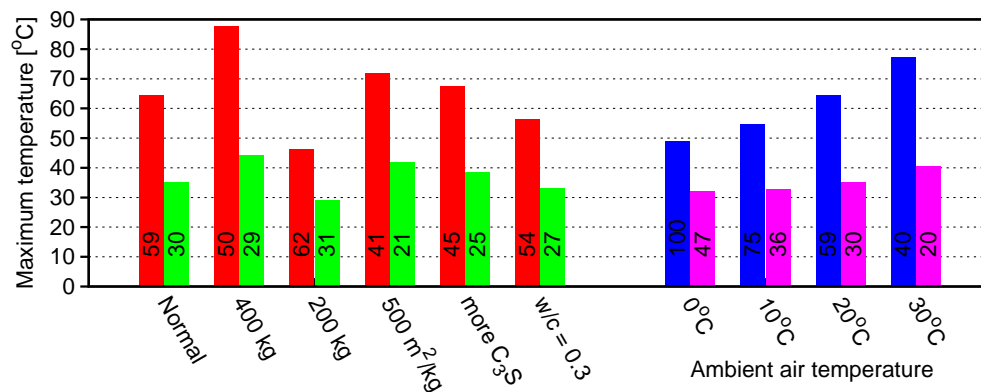


**FIGURE 22.** Maximum temperatures in the beam (left columns) and slab (right columns) when varying individual parameters of cement, concrete, or air temperature. Number in the bar represents time in hours when maximum temperature was reached

and beam. The emphasis was given on the cement physical and chemical properties, utilizing intrinsic reaction enthalpies as a source for liberated heat. The model provides a reasonably accurate tool suited for engineering purposes with appropriate consumption of computation time regarding multi-scale model complexity.

Effect of water evaporation, RH influence on hydration, and changes in concrete thermal conductivity and capacity were not incorporated. Two parameters had to be calibrated in all experiments, representing cycle-time mapping of the hydration model. They were found in the ranges $t_0 \in \langle 0, 3 \rangle$ h and $\beta \in \langle 4.0, 7.8 \rangle$ h/cycle$^2$, covering the role of alkalies or admixtures and possible inaccurate boundary conditions. Several uncertainties remain especially due to a lack of information from construction site. The small-scale experiments show much better agreement due to available details.

## ACKNOWLEDGMENT

## REFERENCES

1. Neville, A. M. *Properties of Concrete*. Wiley, Hoboken, NJ, 1997.

2. Lothenbach, B., Matschei, T., Möschner, G., and Glasser, F. Thermodynamic modelling of the effect of temperature on the hydration and porosity of Portland cement. *Cem. Concr. Res.* **38**(1):1–18, 2008.

3. Bentur, A., and Mitchell, D. Material performance lessons. *Cem. Concr. Res.* **38**(2):259–272, 2008.

4. Nilsson, M. *Thermal Cracking of Young Concrete. Partial Coefficients, Restraint Effects and Influence of Casting Joints*. Licentiate thesis, LuleåUniveristy of Technology, 2000.

5. Schrage, I., and Summer, T. Factors influencing early cracking of high strength concrete, *Proceedings of International RILEM Symposium. Thermal Cracking in Concrete at Early Ages*, pp. 237–244, 1994.

6. Wang, C., and Dilger, D. Prediction of temperature distribution in hardening concrete. *Proceedings of International RILEM Symposium. Thermal Cracking in Concrete at Early Ages*, pp. 21–28, 1994.

7. Bentz, D. P., Waller, V., and de Larrard, F. Prediction of Adiabatic Temperature Rise in Conventional and High-Performance Concretes Using a 3-D Microstructural Model. *Cem. Concr. Res.* **28**(2):285–297, 1998.

8. Estrada, C. F., Godoy, L. A., and Prato, T. Thermo-mechanical behavior of a thin concrete shell during its early age. *Thin-Walled Struct.* **44**(5):483–495, 2006.

9. Park, K.-B., Jee, N.-Y., Yoon, I.-S., and Lee, H.-S. Prediction of Temperature Distribution in High-Strength Concrete Using Hydration Model. *ACI Mater. J.* **105**(2):180–186, 2008.

10. Hellmich, Ch., Mang, H. A., and Ulm, F.-J. Hybrid method for quantification of stress states in shotcrete tunnel shells: combination of 3D in situ displacement measurements and thermochemoplastic material law. *Comput. Struct.* **79**:2103–2115, 2001.

11. Gawin, D., Pesavento, F., and Schrefler, B. Hygro-thermo-chemo-mechanical modelling of concrete at early ages and beyond. Part I: Hydration and hygro-thermal phenomena. *Int. J. Numer. Methods Eng.* **67**(3):299–331, 2006a.

12. Gawin, D., Pesavento, F., and Schrefler, B. Hygro-thermo-chemo-mechanical modelling of concrete at early ages and beyond. Part II: shrinkage and creep of concrete. *Int. J. Numer. Methods Eng.*, **67**(3):332–363, 2006b.

13. Ulm, F.-J., and Coussy, O. Couplings in early-age concrete: From material modeling to structural design. *Int. J. Solids Struct.* **35**(31–32):4295–4311, 1998.

14. NRMCA. *Concrete In Practice*. Technical report, National Ready Mixed Concrete Association, 1978–2007.

15. Barbarulo, R., Peycelon, H., Prené, S., and Marchand, J. Delayed ettringite formation symptoms on mortars induced by high temperature due to cement heat of hydration or late

thermal cycle. *Cem. Concr. Res.* **35**(1):125–131, 2005.

16. Bentz, D. P. *CEMHYD3D: A Three-Dimensional Cement Hydration and Microstructure Development Modeling Package. Version 3.0.* Technical Report, NIST Building and Fire Research Laboratory, Gaithersburg, MD, 2005.

17. Wang, B.-L., and Mai, Y.-W. Transient one-dimensional heat conduction problems solved by finite element. *Int. J. Mech. Sci.* **47**(2):303–317, 2005.

18. Zeman, J., and Šejnoha, M. From random microstructures to representative volume elements. *Modell. Simul. Mater. Sci. Eng.* **15**(4):S325–S335, 2007.

19. Maekawa, K., Chaube, R. P., and Kishi, T. *Modeling of Concrete Performance*. E & FN SPON, London, first edition, 1999.

20. Kada-Benameur, H., Wirquin, E., and Duthoit, B. Determination of apparent activation energy of concrete by isothermal calorimetry. *Cem. Concr. Res.* **30**(2):301–305, 2000.

21. Bentz, D. *CEMHYD3D: A Three-Dimensional Cement Hydration and Microstructure Development Modeling Package. Version 2.0.* Technical Report, NIST Building and Fire Research Laboratory, Gaithersburg, MD, 2000.

22. Bentz, D. *A Three-Dimensional Cement Hydration and Microstructure Program. I. Hydration Rate, Heat of Hydration, and Chemical Shrinkage.* Technical Report, NIST Building and Fire Research Laboratory, Gaithersburg, MD, 1995.

23. Bentz, D. P., Garboczi, E., Haecker, C., and Jensen, O. Effect of cement particle size distribution on performance properties of Portland cement-based materials. *Cem. Concr. Res.* **29**:1663–1671, 1999.

24. Kanit, T., Forest, S.,Galliet, I., Mounoury, V.,

and Jeulin, D. Determination of the size of the representative volume element for random composites: Statistical and numerical approach. *Int. J. Solids Struct.* **40**:3647–3679, 2003.

25. Pane, I., and Hansen, W. Investigation of blended cement hydration by isothermal calorimetry and thermal analysis. *Cem. Concr. Res.* **35**(6):1155–1164, 2005.

26. Papadakis, V. Effect of fly ash on Portland cement systems: Part I. Low-calcium fly ash. *Cem. Concr. Res.* **29**(11):1727–1736, 1999.

27. Robeyst, N., Gruyaert, E., and Belie, N. D. *Advances in Construction Materials 2007: Ultrasonic and Calorimetric Measurements on Fresh Concrete with Blast-Furnace Slag*, Springer, Berlin, pp. 497–504, 2007.

28. Snelson, D. G., Wild, S., and O'Farrell, M. Heat of hydration of Portland Cement-Metakaolin-Fly ash, (PC-MK-PFA) blends. *Cem. Concr. Res.* **38**(6):832–840, 2008.

29. Lienhard, J., and Lienhard, J. *A Heat Transfer Textbook*. Phlogiston Press, Cambridge, 2008.

30. Hughes, T. *The Finite Element Method–Linear Static and Dynamic Finite Element Analysis*. Dover Publishers, New York, 2000.

31. Bentz, D. Transient Plane Source Measurements of the Thermal Properties of Hydrating Cement Pastes. *Mater. Struct.* **40**(10):1073–1080, 2007.

32. Bernard, O., Ulm, F.-J., and Lemarchand, E. A multiscale micromechanics-hydration model for the early-age elastic properties of cement-based materials. *Cem. Concr. Res.* **33**(9):1293–1309, 2003.

33. Šmilauer, V., and Bittnar, Z. Microstructure-based micromechanical prediction of elastic properties in hydrating cement paste. *Cem. Concr. Res.* **36**(9):1708–1718, 2006.